Supporting Information Text

Is F_1-ATPase a rotary motor with nearly 100% efficiency? Quantitative analysis of chemomechanical coupling and mechanical slip

Tomonari Sumi[1,2] **and Stefan Klumpp**[3,4]

[1]Research Institute for Interdisciplinary Science, Okayama University, 3-1-1 Tsushima-Naka, Kita-ku, Okayama 700-8530, Japan.
[2]Department of Chemistry, Faculty of Science, Okayama University, 3-1-1 Tsushima-Naka, Kita-ku, Okayama 700-8530, Japan.
[3]Institute for the Dynamics of Complex Systems, University of Göttingen, Friedrich-Hund-Platz 1, 37077 Göttingen, Germany
[4]Department Theory and Bio-Systems, Max Planck Institute of Colloids and Interfaces, 14424 Potsdam, Germany

SI Methods

Rotary motor dynamics.

The dynamics of a rotary molecular motor can be described by a continuous-time Markov process. Thus, the probability $P_i(t)$ to find the rotary molecular motor in state i at time t is governed by the following continuous-time master equation:

$$\frac{d}{dt}P_i(t) = -\sum_j \Delta J_{ij}(t), \tag{S1}$$

$$\Delta J_{ij}(t) = P_i(t)\omega_{ij} - P_j(t)\omega_{ji}, \tag{S2}$$

where ω_{ij} is a transition rate from state i to state j, i.e., the number of transitions from i to j per unit time and $\Delta J_{ij}(t)$ is the local excess flux due to the transition from state i to state j. In general, the transition rate ω_{ij} depends on both the external torque, τ , and the molar concentrations $[X]$, where X denotes the molecular species ATP, ADP, or P_i (inorganic phosphate). Thus the transition rates can be given by

$$\omega_{ij} = \omega_{ij}^0 \Phi_{ij}(\tau), \tag{S3}$$

where ω_{ij}^0 is the torque-free transition rate and $\Phi_{ij}(\tau)$ is a torque-dependent factor with $\Phi_{ij}(\tau = 0) = 1$. Moreover, ω_{ij}^0 for binding of an X-molecule depends on the molar concentration $[X]$,

$$\omega_{ij}^0 = \begin{cases} \hat{k}_{ij}[X] & \text{for X-binding} \\ k_{ij} & \text{for X release} \end{cases}. \tag{S4}$$

Here, $\hat{k}_{ij}$ has the dimension $1/(\mu\text{Ms})$ while k_{ij} has the dimension 1/s. In the present study, we assume that only the rotational transitions rates depend on the external torque and also that $\Phi_{ij}(\tau)$ for

the forward (anticlockwise) rotational transitions under the backward torques (toward clockwise rotation direction) has the following form (note that a backward torque τ is taken to be positive):

$$\Phi_{ij}(\tau) = \exp\left[-\tau\theta_{ij}/\tau_{ij}\right], \quad \text{(S5)}$$

$$\Phi_{ji}(\tau) = \exp\left[\tau\left(1-\theta_{ij}\right)/\tau_{ij}\right], \quad \text{(S6)}$$

where τ_{ij} is a torque scale with respect to the torque dependence of the mechanical step transition and θ_{ij} is a torque distribution factor with a value of $0 < \theta_{ij} < 1$ [1].

Calculation details.

In the eight-state model shown by Fig. 1b, the rotation rate V is calculated as $V = V_{15} + V_{73} + V_L + V_T$, where $V_{15} = (2/9)\Delta J_{15}^{st}$ (80° anticlockwise rotation rate), $V_{73} = (1/9)\Delta J_{73}^{st}$ (40° anticlockwise rotation rate), $V_L = (1/3)P_L^{st}\left(\omega_{LL}^{f} - \omega_{LL}^{b}\right)$ (120° anticlockwise slip rotation rate at 0° dwell), and $V_T = (1/3)P_T^{st}\left(\omega_{TT}^{f} - \omega_{TT}^{b}\right)$ (120° anticlockwise slip rotation rate at 80° dwell). Here, ΔJ_{ij}^{st} and P_i^{st} are the local excess flux in the steady state and the state probability, respectively, and ω_{LL}^{f}(and ω_{TT}^{f}) and ω_{LL}^{b}(and ω_{TT}^{b}) are the rates of torque-induced mechanical slip, i.e., 120° rotation transitions, in the loose (and tight) packing state towards the forward and backward directions, respectively. P_L^{st} and P_T^{st} are a sum of the steady-state probabilities in the loose and tight packing states, i.e., $P_L^{st} = P_1^{st} + P_2^{st} + P_3^{st} + P_4^{st}$ and $P_T^{st} = P_5^{st} + P_6^{st} + P_7^{st} + P_8^{st}$, respectively. ω_{LL}^{f} and ω_{LL}^{b} are provided by $\omega_{LL}^{f} = \omega_{LL}^{0}\exp\left[-\tau\theta_{LL}/\tau_{LL}\right]$ and $\omega_{LL}^{b} = \omega_{LL}^{0}\exp\left[\tau\left(1-\theta_{LL}\right)/\tau_{LL}\right]$, respectively, and ω_{TT}^{f} and ω_{TT}^{b} are given in the same manner as ω_{LL}^{f} and ω_{LL}^{b}.

The number of unknown transition rates can be reduced by using the steady-state balance condition [2,3]. The determination of unknown parameters for the transition rates was performed as follows. We first applied the eight-state model [Fig. 1b] to the experimental data of the F1-ATPase observed with a 287-nm probe bead at various nucleotide concentrations [4], which contains the external-torque dependence of the rotation rate *V* [Figs. 2b and 2c] and the ratio of the number of backward rotation steps to the number of forward rotation steps as a function of external torque [Fig. 2d]. Next, we applied the eight-state model with the determined transition rates to calculate ATP-concentration dependences of the rotation rate *V* that have been observed using the 40-nm bead and 1-μm actin as the probe [5]. In these calculations, all the rotation transition rates toward both the forward and backward directions were multiplied by a single-scaling factor to describe the experimental rotation rates *V* in both the cases of the 40-nm bead and 1-μm actin [Fig. 2a] [5]. The change in the rotation rate *V* by applying the single-scaling factor to all the rotation transition rates is qualitatively interpreted as a change in the viscous friction of the probe depending on the probe. It is noted that the usage of the equal scaling factor for these rotation transition rates is useful to keep the steady-state balance condition. The results shown in Figs. 3a, 3b, 3c, and Figs. S2, S3, S4, and S5 are calculated using the set of the transition rate parameters determined using the experimental data with

the 287-nm bead by Toyabe *et al*. [4] The results shown in Figs. S5 do not depend on the scaling factor for the rotation transition rates, thus the set of the transition rates determined by the experimental data with the use of the 287-nm bead [4] was applied to the calculation of Figs. S5. The experimental data shown in Figs. 4 has also been provided by Toyabe and Muneyuki, where they have used a 300-nm bead as the probe [6]. We used the set of the transition rates that was determined using the experimental data observed by the use of 287-nm bead [4] to calculate the results for the ATP synthesis regime shown in Figs. 4 [6]. The eight-state model based on the determined parameters quantitatively described the experimental rotation rate V at the ATP synthesis regime [6], even though no single-scaling factor was applied to the rotation transition rates, as done for the probes of the 40-nm bead and 1-μm actin.

Determination of the transition rate parameters.

The transition rates of our model were determined by comparing its predictions with experimental results following an iterative strategy: We started with initial guesses for the values of the transition rates that satisfy the following assumptions: We assumed that the ATP binding and release rates on the loose packing states (the right-hand side in Fig. 1b) were larger than those on the tight packing states (the left-hand side in Fig. 1b). On the other hand, we assumed that the reaction rates contained in ATP hydrolysis and synthesis on the tight packing states were faster than those on the loose packing states. Then, we applied the eight-state model to calculate V at varying ATP, ADP and Pi concentrations under an external torque free condition and compare with the experimental results [Figs. 2b and 2d]. We updated the transition rate parameters so that the obtained V values agree with the experimental values of V. Using the obtained (force-free) parameters, we next applied the model to the external torque dependencies of V under those nucleotide concentrations [Figs. 2b and 2d] and updated both the chemical and mechanical transition rate parameters. It is noted that, in this parameter determination procedure, we imposed the steady-state balance conditions (Eqs. S7–S11 below) as constraints [2,3]. Based on the determined parameters, we finally calculated the ATP-concentration dependence of V under different probes [Fig. 2a] by applying a single scaling factor on all the mechanical transitions for 80˚ and 40˚ rotations.

The steady state balance conditions for the eight-state model.

In graph theory, the fundamental cycle basis of an undirected graph is a set of simple cycles that forms the basis of the cycle space on the graph. The number of fundamental cycles N_{fc} in a given connected graph is provided as N_e–N_v+1, where N_e is the number of edges and N_v is the number of vertices [7]. In the case of eight-state chemomechanical network model [Fig. 1b], the number of fundamental cycles N_{fc} is five because of N_e=12 and N_v=8. Therefore, five independent relations between the transition rates are provided by the steady state balance condition [2,3]. The five fundamental cycles are displayed

in Fig. S1. These fundamental cycles provide the following equations for satisfying the steady state balance condition:

(1) Cycle <12341>

$$k_{12}k_{23}\hat{k}_{34}\hat{k}_{41}/\hat{k}_{21}k_{14}k_{43}\hat{k}_{32}=1. \quad \text{(S7)}$$

(2)Cycle<56785>

$$k_{56}k_{67}\hat{k}_{78}\hat{k}_{85}/\hat{k}_{65}k_{58}k_{87}\hat{k}_{76}=1. \quad \text{(S8)}$$

(3)Cycle<1231>

$$k_{12}k_{23}\hat{k}_{31}/\hat{k}_{21}k_{13}\hat{k}_{32}=K_{eq}. \quad \text{(S9)}$$

(4)Cycle <5785>

$$\hat{k}_{75}k_{58}k_{87}/k_{57}\hat{k}_{78}\hat{k}_{85}=K_{eq}. \quad \text{(S10)}$$

(5)Cycle <15731>

$$\omega_{15}^{0}k_{57}\omega_{73}^{0}\hat{k}_{31}/\omega_{51}^{0}k_{13}\omega_{37}^{0}\hat{k}_{75}=1. \quad \text{(S11)}$$

We can use these equations to reduce the number of unknown transition rates.

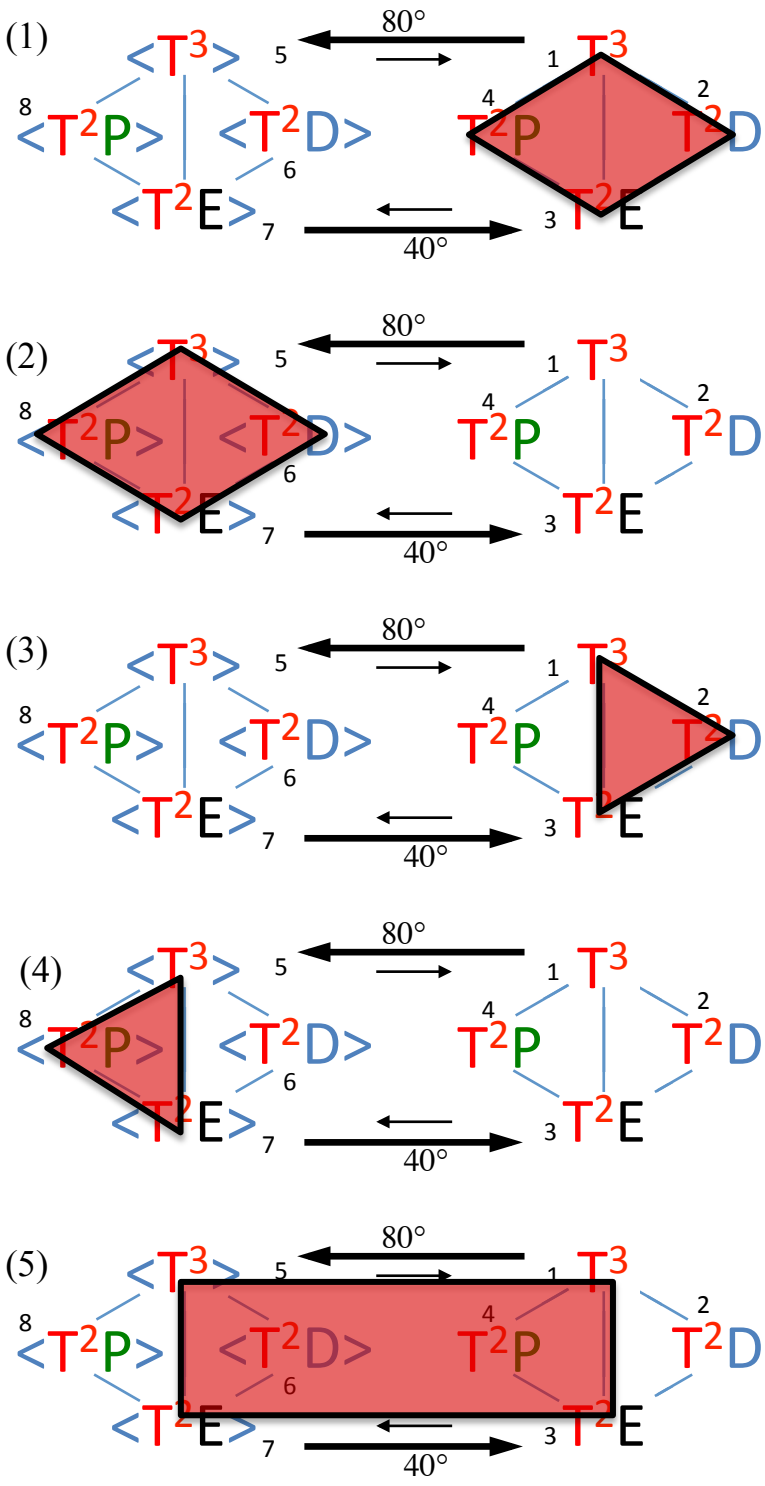

Figure S1. Five fundamental cycles for the eight-state network model. The transparent reds surrounding by black bold line in each figure indicates the fundamental cycle.

Transition rates determined by fitting to the experimental data for F1-ATPase with the 287-nm bead [4].

Table S1. The chemical transition rates in the eight-state network model.

Parameters	Meaning	Values
k_{12}	Pi release at the loose packing state	0.0030 s^{-1}
$\hat{k}_{21}$	Pi binding at the loose packing state	5.0 x 10^{-9} $(\mu Ms)^{-1}$
k_{43}	Pi release at the loose packing state	0.040 s^{-1}
$\hat{k}_{34}$	Pi binding at the loose packing state*	8.8 x 10^{-9} $(\mu Ms)^{-1}$
k_{14}	ADP release at the loose packing state	0.010 s^{-1}
$\hat{k}_{41}$	ADP binding at the loose packing state	5.0 x 10^{-9} $(\mu Ms)^{-1}$
k_{23}	ADP release at the loose packing state	0.040 s^{-1}
$\hat{k}_{32}$	ADP binding at the loose packing state*	2.7 x 10^{-9} $(\mu Ms)^{-1}$
k_{13}	ATP release at the loose packing state	525 s^{-1}
$\hat{k}_{31}$	ATP binding at the loose packing state	28 $(\mu Ms)^{-1}$
k_{56}	Pi release at the tight packing state	500 s^{-1}
$\hat{k}_{65}$	Pi binding at the tight packing state	0.20 $(\mu Ms)^{-1}$
k_{87}	Pi release at the tight packing state	500 s^{-1}
$\hat{k}_{78}$	Pi binding at the tight packing state*	0.24 $(\mu Ms)^{-1}$
k_{58}	ADP release at the tight packing state	25000 s^{-1}
$\hat{k}_{85}$	ADP binding at the tight packing state	77.5 $(\mu Ms)^{-1}$
k_{67}	ADP release at the tight packing state*	20500 s^{-1}
$\hat{k}_{76}$	ADP binding at the tight packing state	77.5 $(\mu Ms)^{-1}$
k_{57}	ATP release at the tight packing state	1.0 x 10^{-10} s^{-1}
$\hat{k}_{75}$	ATP binding at the tight packing state*	7.4 x 10^{-5} $(\mu Ms)^{-1}$

* Determined by the steady state balance condition.

Table S2. The rotation transition rates in the eight-state network model.

Parameters	Meaning	Values
ω_{15}^{0}	Forward (anticlockwise) 80˚ rotation transition	1939 s^{-1}
ω_{51}^{0}	Backward (clockwise) 80 ˚ rotation transition	0.096 s^{-1}
τ_{15}	Torque dependence for the 80˚ rotation transition	2.95 pN nm/rad
θ_{15}	Torque distribution factor for the 80˚ rotation transition	0.35
ω_{73}^{0}	Forward (anticlockwise) 40˚ rotation transition	66.8 s^{-1}
ω_{37}^{0}	Backward (clockwise) 40˚ rotation transition	0.098 s^{-1}
τ_{73}	Torque dependence for the 40˚ rotation transition	5.90 pN nm/rad
θ_{73}	Torque distribution factor for the 40˚ rotation transition	0.42
ω_{LL}^{0}	Symmetric 120˚ rotation rate at the loose packing state	0.0060 s^{-1}
τ_{LL}	Torque dependence for the 120˚ slip rotation at the loose packing state	1.97 pN
θ_{LL}	Load distribution factor for the 120˚ slip rotation at the loose packing state	0.79
ω_{TT}^{0}	The symmetric 120˚ rotation rate at the tight packing state	0.0060 s^{-1}
τ_{TT}	Torque dependence factor for the 120˚ slip rotation at the tight packing state	1.97 pN
θ_{TT}	Load distribution factor for the 120˚ slip rotation at the tight packing state	0.79

Appendix

The detailed balance condition in the model by Kawaguchi *et al*.

The model by Kawaguchi *et al*. yields endothermic and exothermic behavior for the ATP hydrolysis and synthesis regime, respectively [8]. In the following, we show that within this model, the stall condition results in an equilibrium state, in contrast to what our model predicts and also in contrast to the experimental result by Toyabe *et al*. [4]. In their model, chemical transitions are represented by switching between spatially shifted potentials $U_n(x)$ and $U_{n+1}(x)$. The corresponding transition rate satisfy local detailed balance by construction:

$$f_n^+(x) = k_0 \exp\left[-\frac{q}{k_B T}\{U_{n+1}(x) - U_n(x) - \Delta\mu\}\right],$$

$$f_{n+1}^-(x) = k_0 \exp\left[-\frac{1-q}{k_B T}\{U_n(x) - (U_{n+1}(x) - \Delta\mu)\}\right].$$

Making use of the periodicity, the probability distribution can be derived. Writing, $x_{n+1} = x_n - \frac{2}{3}\pi$, we rewrite the switching rates between the potentials $U_n(x_n)$ and $U_{n+1}\left(x_n - \frac{2}{3}\pi\right)$ as follows:

$$f_n^+(x_n) = k_0 \exp\left[-\frac{q}{k_B T}\left\{\left(U_{n+1}\left(x_n - \frac{2}{3}\pi\right) - \Delta\mu\right) - U_n(x_n)\right\}\right],$$

$$f_{n+1}^-(x_n) = k_0 \exp\left[-\frac{1-q}{k_B T}\left\{U_n(x_n) - \left(U_{n+1}\left(x_n - \frac{2}{3}\pi\right) - \Delta\mu\right)\right\}\right].$$

Then, the probability distribution functions given by $U_n(x_n)$ and $U_{n+1}\left(x_n - \frac{2}{3}\pi\right)$ are respectively given by

$$P_n(x_n) = C_n \exp\left[-\frac{1}{k_B T}(U_n(x_n) - x_n F)\right],$$

$$P_{n+1}(x_n) = C_{n+1} \exp\left[-\frac{1}{k_B T}\left\{U_{n+1}\left(x_n - \frac{2}{3}\pi\right) - \left(x_n - \frac{2}{3}\pi\right)F\right\}\right],$$

where the normalization constants are provided by

$$C_n = \int dx \exp\left[-\frac{1}{k_B T}(U_n(x) - xF)\right],$$

$$C_{n+1} = \int dx \exp\left[-\frac{1}{k_B T}\left\{U_{n+1}\left(x - \frac{2}{3}\pi\right) - \left(x - \frac{2}{3}\pi\right)F\right\}\right]$$

$$= C_n.$$

Thus, the probability distribution has the form of an equilibrium distribution in the potential $U_n(x_n)$ and under force *F*, but because of the additional chemical potential $\Delta\mu$, fluxes are generally not zero, so this distribution does not correspond to a real equilibrium. Under two conditions, however, we obtain equilibrium states, which we show now for the totally asymmetric allosteric model (TASAM) with *q*=0. In that case, we obtain

$$P_n(x_n)f_n^+(x_n) = C_n k_0 \exp\left[-\frac{1}{k_B T}(U_n(x_n) - x_n F)\right],$$

$$P_{n+1}(x_n)f_{n+1}^-(x_n) = C_{n+1} k_0 \exp\left[-\frac{1}{k_B T}\left\{U_n(x_n) - \left(x_n - \frac{2}{3}\pi\right)F + \Delta\mu\right\}\right].$$

If $\Delta\mu = 0$ and $F = 0$, we obtain the excess switching flux,

$\Delta J_n(x_n) \equiv P_n(x_n)f_n^+(x_n) - P_{n+1}(x_n)f_{n+1}^-(x_n) = 0,$

indicating that the model by Kawaguchi *et al*. satisfies the detailed balance condition at all angles under the thermodynamic equilibrium. Likewise, for $F = \frac{3}{2\pi}\Delta\mu$, we obtain

$$P_n(x_n)f_n^+(x_n) = C_n k_0 \exp\left[-\frac{1}{k_B T}\left\{U_n(x_n) - x_n \frac{3}{2\pi}\Delta\mu\right\}\right],$$

$$P_{n+1}(x_n)f_{n+1}^-(x_n) = C_{n+1} k_0 \exp\left[-\frac{1}{k_B T}\left\{U_n(x_n) - x_n \frac{3}{2\pi}\Delta\mu\right\}\right],$$

that result in

$\Delta J_n(x_n) = P_n(x_n)f_n^+(x_n) - P_{n+1}(x_n)f_{n+1}^-(x_n) = 0.$

This result indicates that the model by Kawaguchi *et al*. also satisfies the detailed balance condition at all angles under the stall torque condition, which thus is an equilibrium condition, and yields the perfect free-energy transduction efficiency $W_{\text{stall}} = \Delta\mu$. This result is not consistent with the experimental results by Toyabe *et al*. [4], as shown by Fig. 3 in the main text.

Numerical Results

Stall torques determined by the relationship between the chemomechanical-coupling rotation rate V_{chem} and mechanical-slip rotation rate V_{slip}.

In the main text, we showed that the stall torque τ_{stall}–which was related to the quasi-static maximum work given by $W_{\text{stall}} = (2\pi/3)\tau_{\text{stall}}$–depended on the concentrations of ATP and ADP even if $\Delta\mu$ was constant [see Fig. 3a], and also that the value of τ_{stall} became smaller than the tight-coupling-limit value of τ_{stall} with increasing $\Delta\mu$ [see Fig. 3b]. These observations imply that F_1-ATPase is not an ideal tight-coupling rotary motor with 100% chemomechanical free-energy transduction efficiency. In the following, we demonstrate that the deviation of τ_{stall} from the tight coupling limit, which depends on the nucleotide condition, is not caused by either an artifact on the data analysis or an experimental error, but is rather interpreted by the relationship between the chemomechanical-coupling rotation rate V_{chem} and the mechanical-slip rotation rate V_{slip}, where V_{chem} is the rotation rate caused by the chemomechanical coupling, i.e., $V_{15} + V_{73}$, corresponding to the rotation rate the non-slip model, and V_{slip} is the rate of rotations caused by the mechanical slip, i.e., $V_L + V_T$ (see **Calculation details** above).

First of all, we examine the external torque dependencies of the experimental [4] and

theoretical rotation rates in the vicinity of the stall torque at under constant $\Delta\mu$ conditions [Fig. S2a] and varying $\Delta\mu$ conditions [Fig. S2c] (with the same nucleotide conditions as in Figs. 3a and 3b, respectively). We observe in Fig. S2a that all the rotation rates intersect approximately in a single point at a rate slightly lower than zero under the constant $\Delta\mu$ condition, while we observe in Fig. S2c that under the varying conditions, the rotation rates are parallel to each other and have approximately the same negative slope.

As we pointed out in the main text, in the case with mechanical slip, the stall torque is determined by the condition, $V = V_{\mathrm{chem}} + V_{\mathrm{slip}} = 0$. In Figs. S2b and S2d, V_{chem} and $\left|V_{\mathrm{slip}}\right|$ are shown as functions of the external torque. The stall torques are then determined to be the external torques at which V_{chem} and $\left|V_{\mathrm{slip}}\right|$ are crossing each other. In Fig. S2b, we can see that all the curves of the rotation rate V_{chem} given by the non-slip model seem to become zero at the identical stall torque τ_{stall} determined by $\tau_{\mathrm{stall}} = \left(3/2\pi\right)\Delta\mu$; this reflects the nearly tight-coupling-limit behavior of the non-slip model. We find in Fig. S2b that the lowest and second lowest values of stall torque τ_{stall} are obtained for the nucleotide conditions where [ATP] (=[ADP]) is 0.08 and 0.4 μM, respectively. The lowest and second lowest values of $W_{\mathrm{stall}} = \left(2\pi/3\right)\tau_{\mathrm{stall}}$ shown in Fig. 3a are given by the determined lowest and second lowest values of stall torque τ_{stall} at each nucleotide condition, respectively. These observations indicate that the large deviation of $W_{\mathrm{stall}} = \left(2\pi/3\right)\tau_{\mathrm{stall}}$ from the maximal work in the tight-coupling limit, $\Delta\mu$, is attributable to the smaller negative slope in the V_{chem} curve as seen in Fig. S2b.

On the basis of Fig. S2d, the stall torque τ_{stall} by the eight-state model is determined to be the external torque at which V_{chem} and $\left|V_{\mathrm{slip}}\right|$ are crossing each other, while τ_{stall} by the non-slip model corresponds to that at which V_{chem} becomes zero. This observation indicates that the difference in the stall torques between by the eight-state model and by the non-slip model becomes large as $\Delta\mu$ increases, i.e., [ADP] and/or [Pi] decrease because of the positive slope of the $\left|V_{\mathrm{slip}}\right|$ curve. These numerical results demonstrate that the nucleotide-concentration dependencies of the stall torque τ_{stall} as well as the quasi-static maximum work $W_{\mathrm{stall}} = \left(2\pi/3\right)\tau_{\mathrm{stall}}$ surely exist and are attributable to the relationship between V_{chem} and V_{slip}.

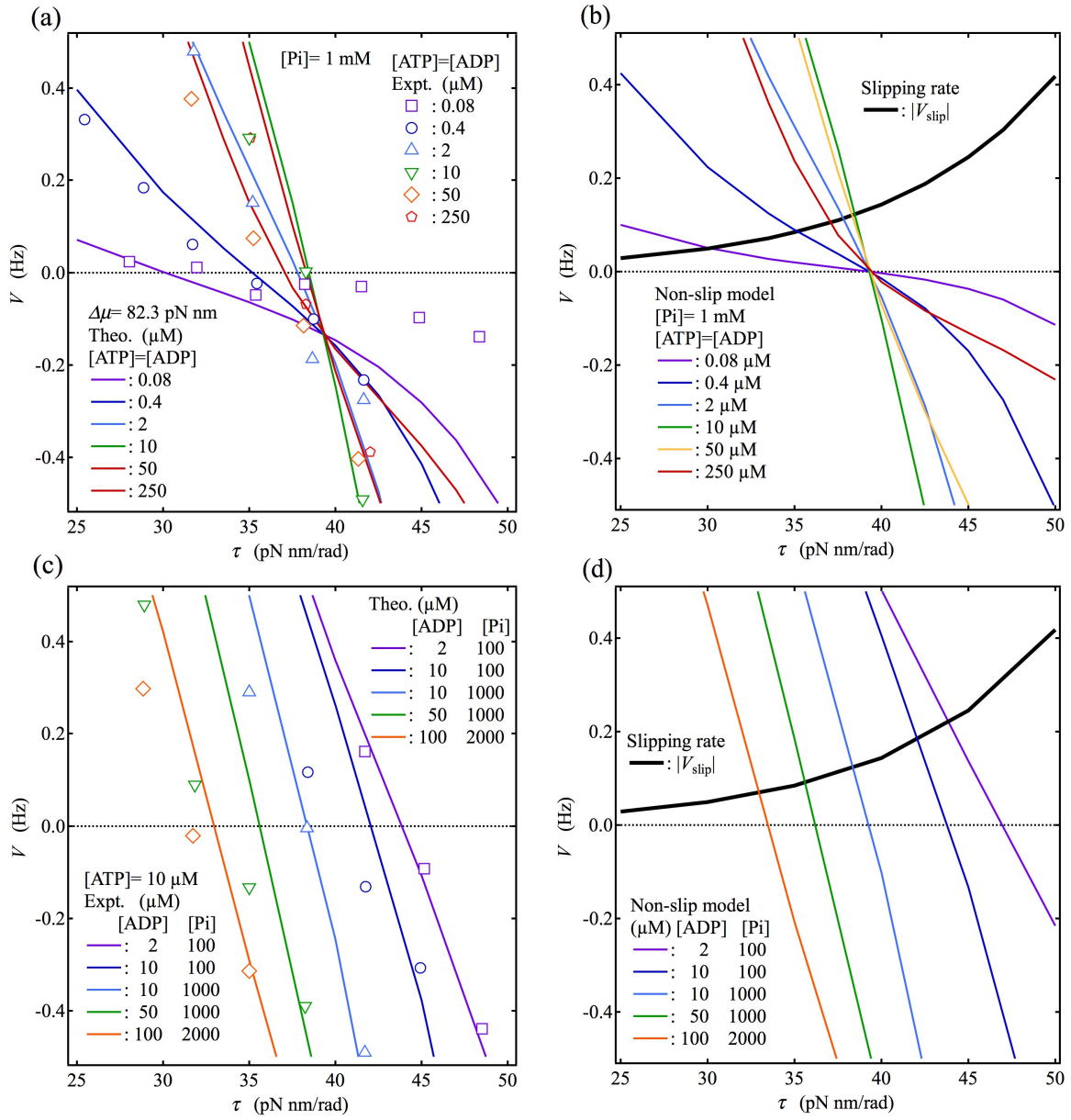

Figure S2. External torque dependence of the rotation rate at the stall torque region (a, b) under the constant $\Delta\mu$ condition corresponding to Fig. 2b and (c, d) at the varying $\Delta\mu$ conditions corresponding to Fig. 2c. In Figs. S2a and S2c, the comparisons between the experimental data [4] and the results obtained from the eight-state model are shown. In Figs. S2b and S2d, the torque-dependent rotation rates, that are obtained from the non-slip model V_{chem} purely driven by the chemomechanical coupling and the absolute values of the contribution to the rotation rate due to the mechanical slip V_{slip}, are shown in order to understand how the stall torque τ_{stall} is determined at each nucleotide condition.

Quasi-static maximum work due to 120º anticlockwise rotation W_{stall} at the different constant $\Delta\mu$ conditions.

For the comparison with Fig. 3a, we show $W_{\mathrm{stall}} = (2\pi/3)\tau_{\mathrm{stall}}$ as a function of the concentrations of ATP and ADP (a) under the condition with [ATP]=10 x [ADP] and [Pi]=1 mM and (b) under the condition with [ATP]=[ADP] and [Pi]=10 mM. The constant $\Delta\mu$ value used in Fig. S3a is larger than that in Fig. S3b. Thus, the deviations from the non-slip model values of W_{stall} in Fig. S3a is larger than that in Fig. S3b. This result is consistent with the $\Delta\mu$-dependence of the deviation of W_{stall} from the non-slip model shown in Fig. 3b. In addition, the characteristic upward convex curvatures on W_{stall} are commonly observed in these figures.

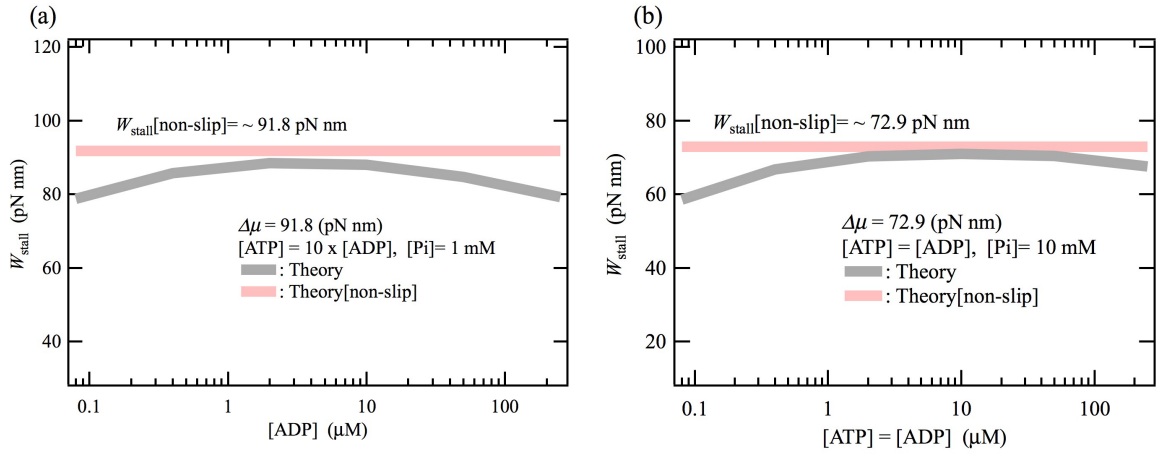

Figure S3. Quasi-static maximum work due to 120º anticlockwise rotation, $W_{\mathrm{stall}} = (2\pi/3)\tau_{\mathrm{stall}}$, as a function of the concentrations of ATP and ADP (a) under the condition [ATP]=10 x [ADP] and [Pi]=1 mM and (b) under the condition [ATP]=[ADP] and [Pi]=10 mM. In Figs. S3a and S3b, the results without the mechanical slip transitions, i.e., the non-slip model values, W_{stall}[non-slip], are also shown as red thick lines.

$\Delta\mu$-dependence of internal heat dissipation $Q_{\mathrm{motor}}/\Delta\mu$.

Figure S4 shows the $\Delta\mu$-dependence of the internal heat dissipation $Q_{\mathrm{motor}}/\Delta\mu$ under the stall torque condition, which is the same as in Fig. 3b. Q_{motor} is always smaller than $\Delta\mu$ and $Q_{\mathrm{motor}}/\Delta\mu$ increases as $\Delta\mu$ increases.

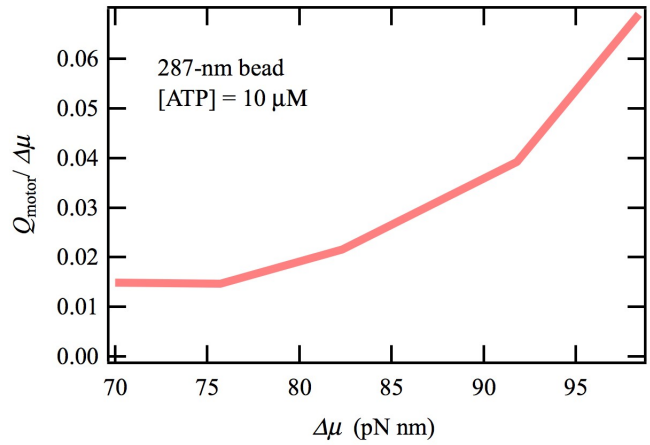

Figuer S4. $\Delta\mu$-dependence of the internal heat dissipation $Q_{\mathrm{motor}}/\Delta\mu$ under the stall torque condition of Fig. 3b.

Mechanochemical coupling efficiency during 120º clockwise rotation.

Figures S5 shows the ratio of the rate of ATP synthesis to the forced clockwise rotation rate divided by three, $\Delta J[\mathrm{hydrolysis}]/(3|V|)$, i.e., a mechanochemical coupling efficiency or an ATP synthesis efficiency, as a function of the rotation rate (a) under the condition with [ATP]= 200 nM, [ADP]= 100 μM, and [Pi]= 10 mM and (b) under the condition with [ATP]=[ADP]= 10 μM, and [Pi]= 1 mM. The former and latter conditions correspond to a physiological condition [9] and the experimental condition [6] as used in Figs. 4, respectively. The non-slip model exhibits almost perfect coupling efficiency between the forced clockwise rotation and ATP synthesis, while the eight-state model yields an imperfect mechanochemical coupling due to the mechanical slipping caused by high external torque. The result shown in Fig. S5a is qualitatively consistent with the experimentally determined efficiency of ~77% under forced 10-Hz clockwise rotation [9]. This observation also provides support for the existence of the mechanical slip rotation under high external torque. In Fig. S5b, we observe a lower mechanochemical coupling efficiency than shown in Fig. S5a. This is because $\Delta\mu = 82.3$ pN nm in (b) is higher than $\Delta\mu = 47.3$ pN nm in (a), with the result that a higher external torque is required in (b) than in (a) to force the reverse rotation.

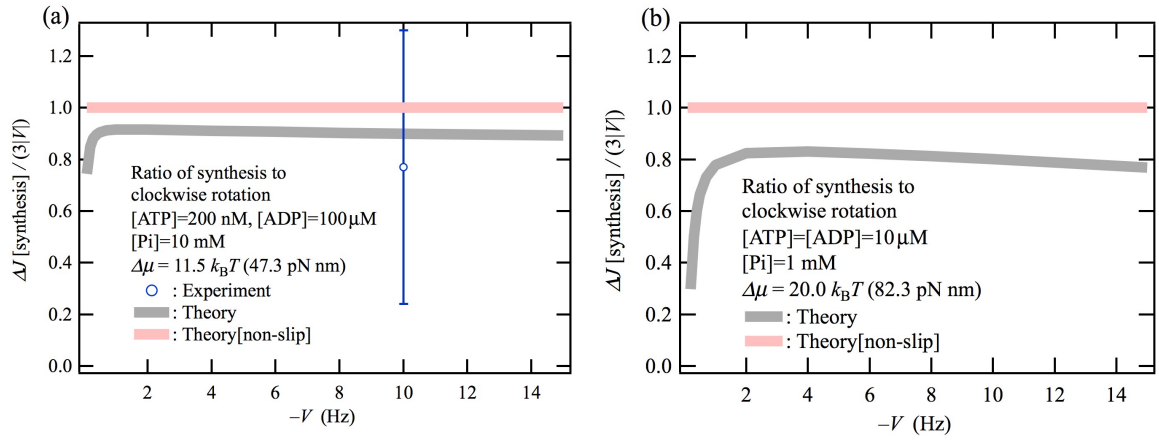

Figure S5. The ratio of the number of ATP synthesis to the forced clockwise rotation rate divided by three, $\Delta J[\text{synthesis}]/(3|V|)$, i.e. a mechanochemical coupling efficiency or an ATP synthesis efficiency, as a function of the rotation rate (a) at [ATP]= 200 nm, [ADP]= 100μM, and [Pi]= 10 mM and (b) at [ATP]=[ADP]= 10 μM, and [Pi]= 1 mM. The experimentally determined mechanochemical coupling efficiency upon ATP synthesis under forced 10-Hz clockwise rotation by Rondelez *et al.* [9] is shown in Fig. S5a.

Main cycles of F1-ATPase at different ATP concentrations and external torques.

The reaction scheme of F_1-ATPase can be examined using the main excess fluxes on the chemomechanical network. Figures S6 shows the main local fluxes for F_1-ATPase with the use of 287-nm beads [4] under torque-free condition at nucleotide concentrations of (a) [ATP]=2 mM and (b) [ATP]=2 μM and (c) under the stall-torque condition with [ATP]=2mM and (d) under a super stall torque with [ATP]=0.2 μM, [ADP]=0.1 mM, and [Pi]=10 mM so that the forced clockwise rotation rate is 10 Hz. The condition in Fig. S6d corresponds to the maximal rate of ATP synthesis that has been biochemically determined for a F_oF_1 enzyme at room temperature [9]. The red arrows indicate normalized local fluxes exceeding 0.1 and the blue arrows indicate the other normalized local fluxes larger than 0.05, where the normalized local flux means the value of local flux divided by the sum of all the local fluxes. The red numbers beside the state numbers indicate the state probabilities. Figure S6a shows that the 40˚ anticlockwise forward rotation occurs in the main working cycle |158731> after the Pi release (the 8-to-7 transition) that follows the ADP release (the 5-to-8 transition). In the chemomechanical network model proposed by the present work [Fig. 1b], an alternative working cycle |156731>, where the 40˚ anticlockwise forward rotation takes place after the ADP release (the 5-to-8 transition) that follows the Pi release (the 8-to-7 transition), is also included, but the cycle |156731> does not appear as the main working cycle. The timing of Pi release in the main working cycle |158731> is consistent with the experimental observation by Watanabe *et al.* [10] and the molecular dynamics simulation by Okazaki *et al.* [11] It is remarkable that the following result is derived from the

network modeling: the cycle |158731> rather than the cycle |156731> is necessary to describe the external torque dependence of the rotation rate V at various nucleotide concentrations of ATP, ADP, and Pi shown in Figs. 2b and 2c.

Comparing Figs. S6a and S6b, we find that the main working cycle does not depend on the ATP concentration whereas the state probabilities do. At the high ATP concentration of 2 mM [Fig. S6a], state 7 (<T^2E>) has the highest probability (~0.8), indicating that the 40° rotation triggered by the Pi release is the rate-limiting transition. In addition, the second-highest probability (~0.1) for state 8 (<T^2P>) implies that Pi release (the 8-to-7 transition) is the second rate-limiting process. This slow Pi release agrees with the molecular dynamics simulation result by Okazaki *et al.* [11] At the low ATP concentration of 2 μM [Fig. S6b], state 3 (T^2E) has the highest state probability of about 0.6, indicating that ATP binding is the rate-limiting process.

Figure S6c shows that frequent ATP binding and release between states 1 (T^3) and 3 (T^2E) are the main local fluxes under the stall-torque condition at high ATP concentration of 2 mM. Such a fast ATP release would be important to achieve the high ATP-synthesis rate by forced clockwise rotation. Figure S6d indicates that the reaction scheme of ATP synthesis corresponds to the reversal of the ATP hydrolysis process and also that the ADP binding and release between states 6 (<T^2D>) and 7 (<T^2E>) also appear as large local fluxes. The high state probability of ~0.9 for state 3 (T^2E) indicates that the 40° clockwise rotation forced by external torque is the rate-limiting process for ATP synthesis and it triggers Pi binding (the 7-to-8 transition) as well as the ADP binding and release between states 6 (<T^2D>) and 7 (<T^2E>).

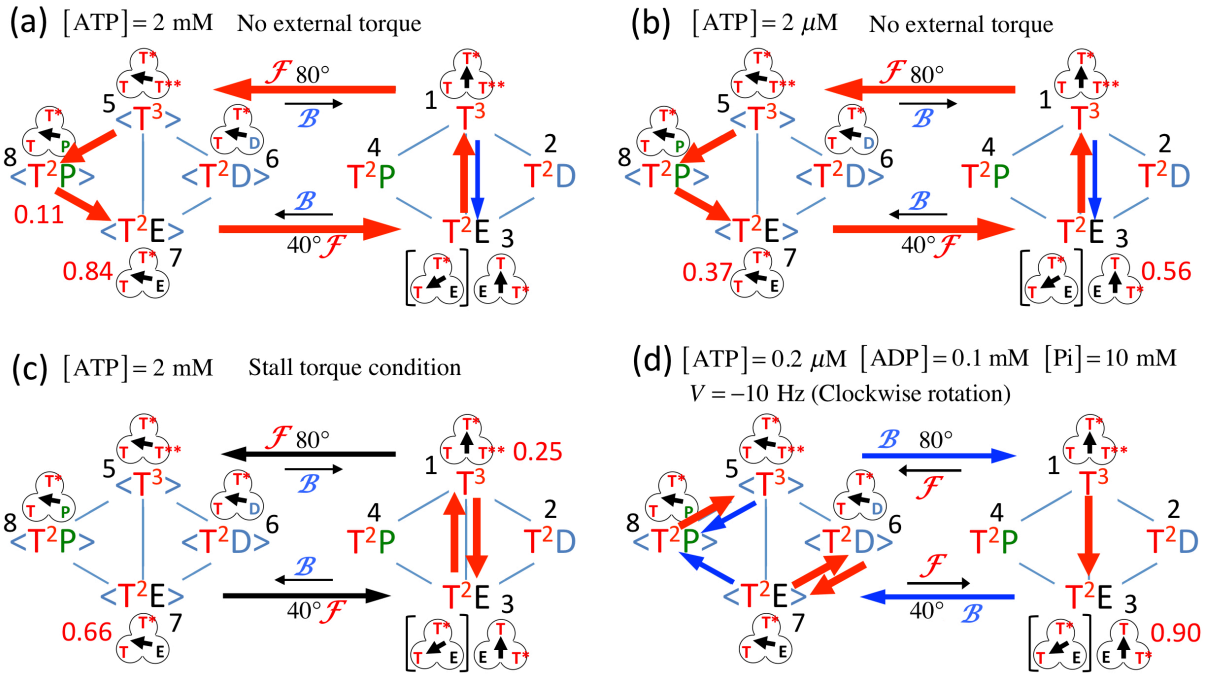

Figure S6. Main local fluxes of F_1-ATPase under various conditions. (a) High ATP concentration of 2 mM and (b) low ATP concentration of 2 μM, under the external-torque-free condition, (c) high ATP concentration of 2 mM under the stall torque, and (d) an ATP-synthesis condition under the superstall torque such that the clockwise rotation rate is -10 Hz wherein [ATP]= 0.2 μM, [ADP]= 0.1 mM, and [Pi]= 10 mM. The condition in Fig. S6d corresponds to the maximum rate of ATP synthesis that has been biochemically determined for a F_oF_1 enzyme at room temperature [9]. The red arrows indicate normalized local fluxes larger than 0.1, while the blue arrows indicate the other normalized local fluxes larger than 0.05, where the normalized local flux is calculated as the value of the local flux divided by the sum of all the local fluxes. The red numbers beside state number indicate the state probabilities. The results shown here are based on the experimental results provided by Toyabe *et al.* [4] with the use of 287-nm bead. It is noted that the probability of state depends on the viscous friction of the probe which can be modulated by varying the size of probe.

References

(1) Fisher, M. E.; Kolomeisky, A. B. *Proc. Natl. Acad. Sci. U.S.A.* **1999**, *96* (12), 6597–6602.

(2) Liepelt, S.; Lipowsky, R. *Europhys. Lett.* **2007**, *77* (5), 50002.

(3) Liepelt, S.; Lipowsky, R. *Phys. Rev. Lett.* **2007**, *98* (2), 258102.

(4) Toyabe, S.; Watanabe-Nakayama, T.; Okamoto, T.; Kudo, S.; Muneyuki, E. *PNAS* **2011**, *108* (44), 17951–17956.

(5) Yasuda, R.; Noji, H.; Yoshida, M.; Kinosita, K.; Itoh, H. *Nature* **2001**, *410* (6831), 898–904.

(6) Toyabe, S.; Muneyuki, E. *New J. Phys.* **2015**, *17* (1), 015008.

(7) Wallis, W. D. *A Beginner's Guide to Graph Theory*; Springer Science & Business Media: Boston, MA, 2010.

(8) Kawaguchi, K.; Sasa, S.-I.; Sagawa, T. *Biophysical Journal* **2014**, *106* (11), 2450–2457.

(9) Rondelez, Y.; Tresset, G.; Nakashima, T.; Kato-Yamada, Y.; Fujita, H.; Takeuchi, S.; Noji, H. *Nature* **2005**, *433* (7027), 773–777.

(10) Watanabe, R.; Iino, R.; Noji, H. *Nat Chem Biol* **2010**, *6* (11), 814–820.

(11) Okazaki, K.-I.; Hummer, G. *PNAS* **2013**, *110* (41), 16468–16473.